Applied Materials Today 44 (2025) 102736

Contents lists available at ScienceDirect

Applied Materials Today

journal homepage: www.elsevier.com/locate/apmt

Cost-efficient phosphor materials with defect-induced luminescence based on sodium chloride and potassium chloride

Xue Yang [a,b,1], Tao Xiong [a,b,1], Yida Zhou [c], Shutao Xu [c], Zongqing Jin [d], Guanjun Xiao [d], Bo Zou [d], Qingqin Ge [e], Nannan Shi [e], Cheng Sun [a,b,*], Ting Wang [a,b,*], Yinan Zhang [d,*]

[a] College of Physical Science and Technology, Dalian University, Dalian 116622, China
[b] Liaoning Engineering Laboratory of Optoelectronic Information Technology, Dalian 116622, China
[c] National Engineering Research Center of Lower-Carbon Catalysis Technology, Dalian Institute of Chemical Physics, Chinese Academy of Sciences, Dalian 116023, China
[d] State Key Laboratory of Superhard Materials, College of Physics, Jilin University, Changchun 130012, China
[e] Thermo Fisher Scientific China, Shanghai 201203, China

ARTICLE INFO

Keywords:
Phosphor
NaCl
KCl
Luminescence
LED

ABSTRACT

In optoelectronic material community, to pursue a phosphor that is both cost efficient and easy-to-produce is key to the next generation luminescence-related devices. In this work, sodium chloride and potassium chloride are used as ideal starting materials, and hydrochloric acid-treated NaCl and KCl samples are successfully synthesized, via a simple hydrothermal synthesis method. Interestingly, photoluminescence emissions are observed in the HCl-treated materials, which is an unprecedented founding. The oxygens that are introduced in the pristine NaCl crystals during the synthesis procedure are believed to be responsible for the emissions, due to the creation of the defect-related energy band. In addition, a fluorescence enhancement on the HCl-treated samples under high pressure is also revealed. Based on the luminescent NaCl and KCl materials, single-element LEDs are manufactured, achieving blue and blue-green emissions, respectively. The variation in the hue of the samples is also illustrated by tuning the photoluminescence excitation wavelength. We believe the scheme proposed in this work that includes a simple treatment on cost-efficient starting materials, together with its underlying physics is of significance in photoluminescence-related material science.

1. Introduction

Luminescent materials are widely used in electronics and optoelectronics [1]. Luminescence can occur as a result of many kinds of excitations, which is expressed as photo-, cathode-, electro-, chemi-, tribo-, X-ray, or sono-luminescence. For example, a lead-free double perovskite photoluminescent material with improved efficiency by alloying sodium cation into $Cs_2AgInCl_6$ was reported [2]. A spin light emitting diode (LED) electroluminescent material was investigated, using chiral induced spin selectivity to generate spin-polarized carriers, and it demonstrated a spin LED with no magnetic or ferromagnetic contact at room temperature [3]. Combining electron diffraction and cathode-luminescence spectroscopy, the correlation between interlayer distortion and local excited luminescence was investigated [4]. Luminescent materials have also been employed in solid-state lighting, display, medical diagnostics, security labeling, energy conversion, lasers, and amplifiers [5–11]. Recently, luminescent materials have been paid much attention due to its huge application demands, especially in the fields of inorganic phosphors, organic materials, quantum dots and perovskite luminescence [12–19]. Besides, several recent works that have been focused on phosphors for LEDs are also reported in literatures [20–24].

Nowadays, most of luminescent materials are based on semiconductors. In order to improve their optical properties, defects are often introduced into the materials to alter the band structures [25]. It is known that the presence of defects can disrupt the local potential fields within the material's bandgap, introducing additional defect energy levels. When these defect energy levels hold electrons and holes, localized energy levels within the bandgap can be created [26–29]. Under certain light excitations, electrons and holes can undergo transitions between the local energy levels and the conduction band minimum, resulting in a recombination and emissions of photons. This process is

* Corresponding authors.
E-mail addresses: suncheng@dlu.edu.cn (C. Sun), wangting1@dlu.edu.cn (T. Wang), zhangyinan@jlu.edu.cn (Y. Zhang).
[1] Xue Yang and Tao Xiong contributed equally to this work.

https://doi.org/10.1016/j.apmt.2025.102736
Received 4 March 2025; Received in revised form 5 April 2025; Accepted 15 April 2025

well known as defect luminescence. Defect-induced photoluminescence (PL) have been widely studied for several advanced applications, [30–32] and recently, defect engineered luminescence through transition metal ion doping has also been reviewed in Ref [33].

For alkali metal halides, such as sodium chloride (NaCl) and potassium chloride (KCl) crystals, they both have large band gaps without any light emissions in the visible regime: NaCl crystal is a wide-gap insulator with a band gap from 8.0 to 9.0 eV, and KCl's band gap ranges from 7.5 to 8.7 eV [34,35]. However, once certain defects are introduced in the insulators, the situation would undergo significant changes, which may potentially transform into semiconductors, with suitable visible light emissions. A common defect is the doping of impurity atoms, another defect is lattice vacancies, and there is also a gap atom defect [36,37]. These defects alter the electronic structure and energy level distribution of the insulator, providing convenient conditions for electronic transitions, thereby allowing the insulator to exhibit semiconductor conductivity to a certain extent [38]. In this work, NaCl and KCl crystals were successfully introduced with defects through a simple synthesize process, and photoluminescence phenomena are observed and characterized.

2. Results and discussions

In this study, we employed a hydrothermal synthesis method to treat pristine NaCl and KCl crystals separately in hydrochloric acid (HCl) solution. The specific procedures are detailed in the experimental section. For clarity and ease of reference in the subsequent text, the pristine NaCl crystal is denoted as 'NaCl-PR', while our HCl-treated NaCl is referred to as 'NaCl-HTS'. Similarly, 'KCl-PR' is for pristine KCl crystals, and 'KCl-HTS' for HCl-treated KCl.

Powder XRD (PXRD) measurements of NaCl-HTS and KCl-HTS were performed to determine the crystal structure of the crystals synthesized in hydrochloric acid, and the resulting spectra are shown in Fig. 1. The data obtained from the XRD of the samples are in good agreement with the standard XRD card of NaCl (JCPDS No. 05–0628) and KCl (JCPDS No. 41–1476). This indicates that no new crystal structures were formed, and the crystal structure as the same as the pristine sample is still well maintained. The sharpness in the diffraction peaks is clearly observed for both samples, confirming the existence of good crystallinity of the samples treated in hydrochloric acid conditions. With a careful examination of the values of the angles for the diffraction peaks, it is observed that the NaCl-HTS sample has a larger angle of 31.76° at (200) than the pristine NaCl (i.e., 31.69°), and also a larger angle of 45.47° at (220) than NaCl-PR (45.45°). Similar effects are also revealed for KCl, where KCl-HTS has angles of 28.37° at (200) and 40.52° at (220), which are both greater than 28.35 ° and 40.51° for KCl-PR. This increasing trend shown in the PXRD patterns indicates a shrink in the crystal lattice for the HCl-treated samples, and this will be further confirmed and addressed by the single crystal X-ray diffraction analysis later in this work.

The XPS results are shown in Fig. 2. The survey-scan XPS spectra of (Fig. 2a) shows the characteristic peaks of sodium and chlorine in NaCl-HTS, and Fig. 2c shows the characteristic peaks of potassium and chlorine in KCl-HTS. In Fig. 2b, the binding energies of 199.89 eV and 198.38 eV are obtained from the contributions of Cl^- $2p_{1/2}$ and $2p_{3/2}$ orbitals, and 1071.56 eV is observed from the 1s orbital of Na^+. Similarly, in Fig. 2d, 200.00 eV and 198.23 eV are determined from Cl^- $2p_{1/2}$ and $2p_{3/2}$ orbitals, and 295.58 and 292.77 eV are derived from the orbitals of K^+ $2p_{1/2}$ and K^+ $2p_{3/2}$. Besides, the peaks within the range of 0–100 eV are also identified and labeled in Fig.S1 in the Supporting Information. The chemical state information about all elements can be derived from the primary peaks indicated in Figs.2. The peaks revealed in the range of 0–100 eV (Fig.S1) are secondary peak structures regarding O, Cl, and Na (or K), providing with no more information. Note that the peaks around 5 eV in the XPS survey spectrum mainly arise from the contributions of the outermost valence electrons of elements such as Na 3s (or K 4s) and Cl 3p

The XPS spectra comparison between HCl-treated and pristine samples is shown in Figs.S2 and S3. Regarding Fig.S2, after hydrochloric acid treatment, the appearance of the additional O peak (labeled O*) is clear evidence that a new O species is occurred, which is attributed to the defect oxygens. In Fig.S3, compared to NaCl-PR, Na and Cl peaks in NaCl-HTS are both shifted to lower binding energy, excluding the existence of the charge transfer; they would otherwise shift towards opposite directions due to the opposite charges for Na and Cl ions. The reason for shifting to the same direction may be accounted for by the introduction of defect oxygens in the HCl-treated samples; in the XPS community, the values for the binding energy in the spectrum are calibrated with the carbon 1s orbital, which can be affected by the surrounding oxygens, and in this work the oxygen environments are different for HCl-treated and pristine samples. The effect of the oxygen on the C 1s orbital was also addressed in Ref [39].

The surface morphology of the samples was characterized by SEM. The morphology at two scales (i.e., 100 μm and 30 μm) are shown in Fig. 3. Based on Fig.3a and 3b, the grain sizes of the crystals of NaCl-HTS and KCl-HTS both range from 5 - 50 μm; the sizes of the HCl-retreated samples are observed to be similar to those of NaCl-PR and KCl-PR, respectively, indicating few changes in the surface morphology. This result correlates well with the aforementioned similarities revealed in the PXRD spectra.

Through above characterizations, it is found that the HCl-treated and pristine NaCl and KCl have basically similar crystal structures, surface chemical states, as well as surface morphologies.

The optical properties of the samples were carefully investigated, and the PL spectra and photoluminescence excitation (PLE) spectra of NaCl-HTS and KCl-HTS are shown in Fig. 4. It is surprisingly interesting that both NaCl-HTS and KCl-HTS samples exhibited light emissions when subjected to ultraviolet irradiations. In Fig. 4a, the steady state PL spectrum of NaCl-HTS shows a blue emission centered at 445 nm with a broad full-width-half-maximum (FWHM) of 60 nm. The PLE spectrum

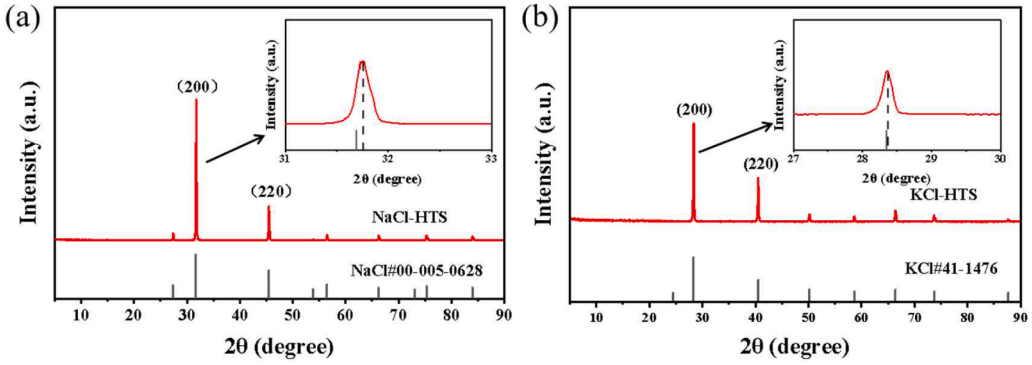

Fig. 1. PXRD patterns of (a) NaCl-HTS, and (b) KCl-HTS.

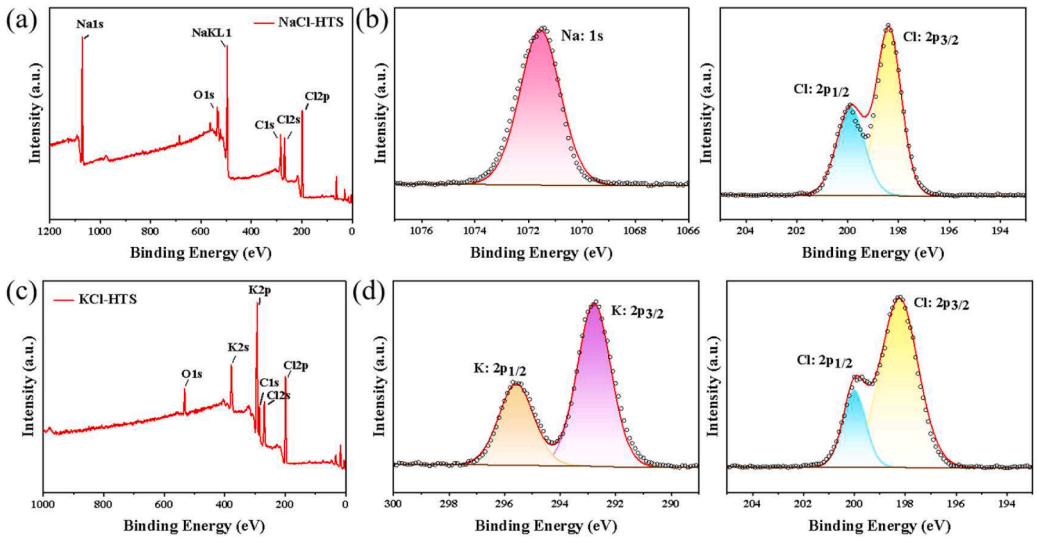

Fig. 2. (a) XPS spectra of NaCl-HTS. (b) High-resolution XPS spectra in Na 1s and Cl 2p regions of NaCl-HTS. (c) XPS spectra of KCl-HTS. (d) High-resolution XPS spectra in K 2p and Cl 2p regions of KCl-HTS.

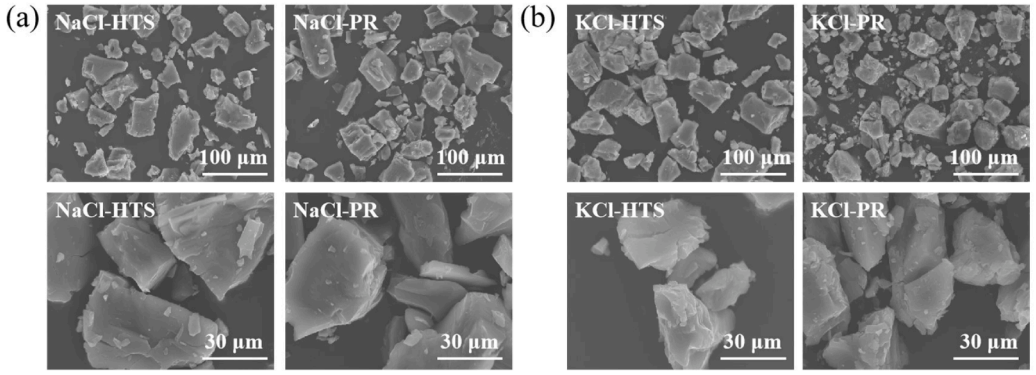

Fig. 3. SEM images of (a) NaCl-HTS and NaCl-PR, and (b) KCl-HTS and KCl-PR in different scales.

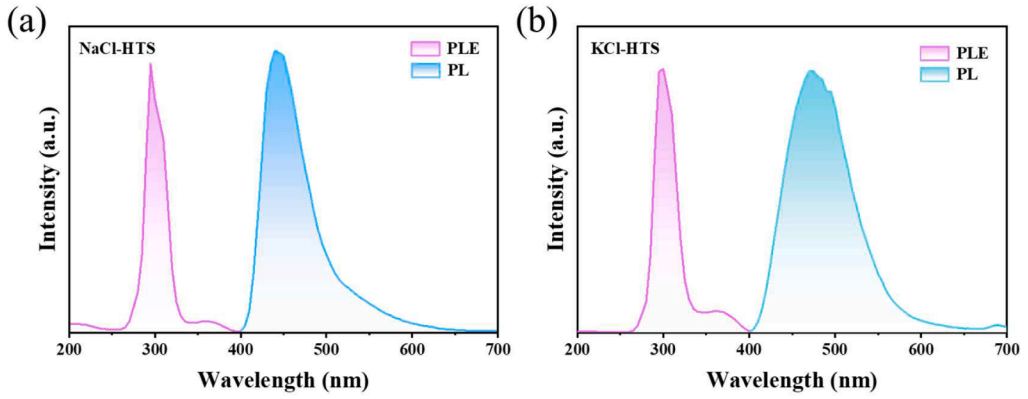

Fig. 4. (a) PL (λ_{ex} = 295 nm) and PLE (λ_{em} = 445 nm) spectra of NaCl-HTS. (b) PL (λ_{ex} = 295 nm) and PLE (λ_{em} = 470 nm) spectra of KCl-HTS.

shows an excitation peak at 295 nm, indicating that the Stokes shift is 150 nm. KCl-HTS has similar luminescent properties, as given in Fig. 4b: a blue-green emission centered at 470 nm is observed in the PL spectrum, with a FWHM of 85 nm. An excitation peak at 295 nm is revealed in the PLE spectrum with a large Stokes shift of 175 nm. In comparison to NaCl-HTS, the emission peak position of KCl-HTS exhibits a notable red shift, indicating lower energy levels created in KCl-HTS than NaCl-HTS. In addition, the quantum efficiency and color purity of the samples were measured to be 57.32 % and 79.75 % for NaCl-HTS, and 44.61 % and 67.67 % for KCl-HTS, respectively. The thermal stability of the phosphor is demonstrated in Fig.S4. The TGA (Thermogravimetric Analysis) curve reveals that up to 300 °C, the synthesized crystal maintains its weight without losing it, indicating good thermal stability.

It is known to the community that pristine NaCl and KCl crystals have no PL emissions, while the obvious PL emissions observed in NaCl-HTS and KCl-HTS are unprecedented. Therefore, there may be some more

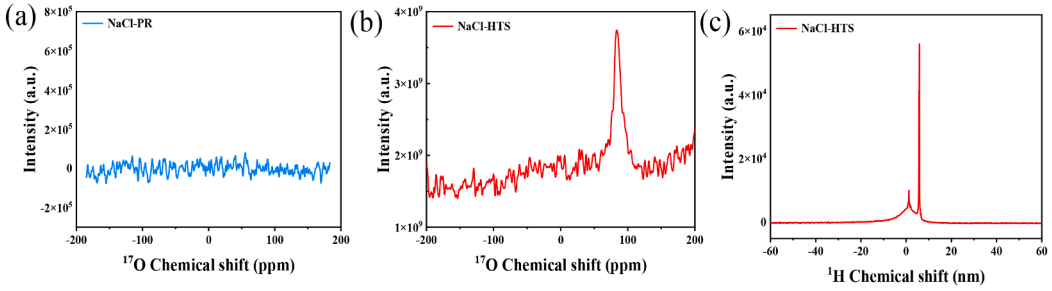

Fig. 5. ^{17}O NMR spectrum of (a) NaCl-PR, and (b) NaCl-HTS. (c) ^{1}H NMR spectrum of NaCl-HTS.

detailed and subtle variations occurring in the HCl-treated samples. To further probe this and shed light on the physics of the luminescence, nuclear magnetic resonance (NMR) spectroscopy was utilized.

As presented in the Fig. 5, it is astonishingly found that there is an explicit oxygen signal revealed in the NaCl-HTS sample (Fig. 5b), whereas none of the oxygen signals is clearly detected in the NaCl-PR sample (Fig. 5a). Recall that the appearance of the additional O peak revealed in XPS spectra (Fig.S2), the substantial difference in these oxygen NMR spectra indicates the undoubtedly presence of oxygen atoms in the NaCl-HTS sample (Fig. 5b), while there is no such oxygens in the pristine NaCl crystals (Fig. 5a). Therefore, it is inferred that the introduction of the oxygens in NaCl-HTS leads to the formation of defects in the previously perfect crystal lattice of NaCl, inducing new energy bands associated with these oxygen-caused defects, and eventually resulting in the PL emission found in the NaCl-HTS sample. The underlying mechanism that is responsible for the luminescence of NaCl-HTS is attributed to the introduction of new energy bands of defects that are correlated to oxygens. Interestingly, although the oxygens affect the energy bands of NaCl-HTS, they do not obviously change the powder crystal structure of the NaCl crystals as discussed in Fig. 1. Besides, based on the ^{1}H NMR spectrum of NaCl-HTS, it is clear that there are two kinds of chemical environments for hydrogen atoms in the HCl-treated sample, corresponding to two chemical shifts observed in Fig. 5c; the ratio of the numbers of these two kinds of hydrogens are determined to $\frac{H(5ppm)}{H(1ppm)} = 3:2$; this will be further discussed together with the SC-XRD results shown below.

To further verify above mechanism and probe this effect caused by the subtle variations from the structural perspective, single crystal X-ray diffraction (SC-XRD) experiments were also performed on the NaCl-HTS sample, from which more sophisticated structural information may be revealed. The CIF file (with the file name 'NaCl-HTS.cif') determined from SC-XRD is provided as an attachment. In the SC-XRD experiment determined crystal structure (Fig. 6a), it is seen that several oxygen atoms are introduced in the NaCl crystal lattice. This is consistent with the appearance of oxygen in the NaCl-HTS sample that was early revealed in the NMR spectra (Fig. 5b). Both experimental results clearly indicate that oxygen atoms were indeed introduced into the body of the NaCl crystal. Therefore, it is believed that the integrated oxygen atoms play a role as defects, causing additional energy bands in the NaCl crystal. Besides, together with the oxygen atoms, several hydrogen atoms are also presented in the NaCl-HTS sample. In details, there are two kinds of hydrogens in the lattice, correlating to the two different chemical environments for hydrogen revealed in the ^{1}H NMR spectrum (Fig. 5c). The hydrogen atom next to chlorine is labeled H_{Cl} and the one in adjacent to oxygen is indicated in H_O. Based on the crystal structure determined from the SC-XRD experiment, the ratio of the numbers of H_{Cl} to H_O is 3:2, and this is surprisingly consistent with the value derived from the previous ^{1}H NMR experiment. As known to the NMR community, the chemical shift of hydrogen is increased, once its neighboring atom's electronegativity is raised; this correlates well to the ^{1}H NMR spectrum (Fig. 5c) where the signal at 5 ppm is H_{Cl}, and the 1 ppm one is H_O. Further, the SC-XRD determined crystal lattice constant of NaCl-HTS is 10.413 Å, which is slightly smaller that of the pristine NaCl (i.e., 11.307 Å), indicating a shrink of the lattice after the NaCl crystal was treated in HCl; this is also consistent with the previous trend observed in the PXRD results (Fig. 1).

Based on above experimental results, a schematic energy diagram is proposed to account for the PL emission from NaCl-HTS (Fig. 6b). The system is first photo-pumped onto the excited state from the ground state, via a 295 nm light. The excited atoms are then relaxed to the defect-induced energy band through a non-radioactive process. The defect-state atoms dissipate their energy in a radioactive fashion, resulting in a PL emission centered at 445 nm.

A detailed theoretical calculation was carried out on the NaCl-HTS sample, using the DFT method. The band gap result is given in Fig.S5, where it was measured to 5.15 eV (i.e., correlating to an absorption wavelength of 241 nm). Compared to the pristine NaCl crystal whose band gap is about 8.0 – 9.0 eV, [34,35] the band gap of the NaCl-HTS crystal with oxygen defects is substantially reduced, resulting in the photoluminescence behavior shown in this work. Note that the discrepancy between the DFT-calculated value (i.e., 241 nm) and the optimal excitation wavelength (i.e., 295 nm) indicated in the PLE experiment (Fig. 4) may be due to the inaccuracy in the estimation of the oxygen atomic concentration in the calculations.

To study the pathways that the defect-state atoms may have undergone through, time-resolved photoluminescence (TRPL) experiments were also done on the NaCl-HTS and KCl-HTS samples (Fig. 7). It is clear that the TRPL decay curves need to fit to a bi-exponential function, indicating that there are two pathways (correlating to two lifetimes) associated with the defect-induced energy band. The decay curves were fitted to a bi-exponential function shown in Eq.1, and the average lifetime was estimated by Eq. 2 [40].

$$I(t) = A_1\exp(-t/\tau_1) + A_2\exp(-t/\tau_2) \quad (1)$$

$$\tau_{ave} = \left(A_1\tau_1^2 + A_2\tau_2^2\right)/\left(A_1\tau_1 + A_2\tau_2\right) \quad (2)$$

where $I(t)$ is the emission intensity at time t, A_1 and A_2 are the weight factors, and τ_1, τ_2 and τ_{ave} are the decay times. With a careful examination of the fitted values, it is found that both samples exhibit a fast and a slow lifetime. In details, NaCl-HTS has a fast lifetime of 6.03 ns and a slow lifetime of 43.64 ns; the average lifetime is 32.90 ns. Similarly, KCl-HTS shows a fast lifetime of 7.22 ns and a slow lifetime of 50.42 ns; the average lifetime is 39.80 ns. The fast lifetime can be ascribed to a radiative recombination process from deep defects, while the slow lifetime can be attributed to a similar phenomenon from shallow defects. Similar effects were observed and addressed in another inorganic material, where two lifetimes were also identified [41].

Besides, the temperature related PL spectra are given in Fig.S6. The emission intensity is decreased with decreasing the temperature from 290 K to 84 K, while the peak position of the PL emission remains unchanged (Fig.S6a). Referring to Fig.S6b, with lowering the temperature, the decreasing trend in the integrated intensity indicates that the radiative recombination is reduced, correlating to the quench of the oxygen defects at low temperature.

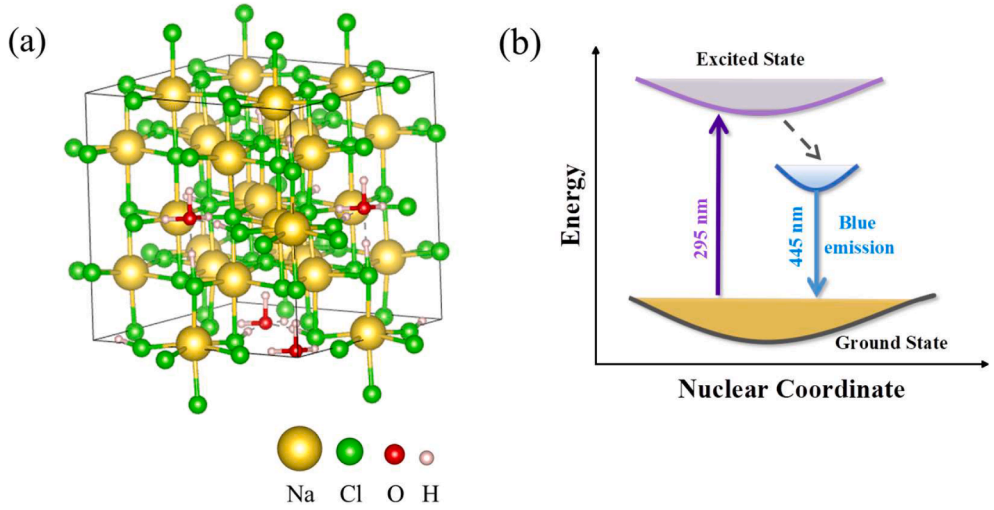

Fig. 6. (a) The crystal structure of NaCl-HTS determined from the SC-XRD experiment. (b) Schematic energy diagram and PL mechanism for NaCl-HTS.

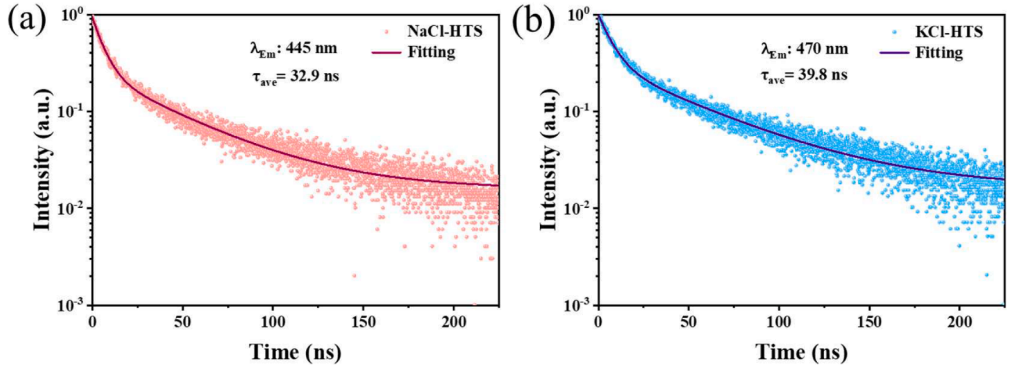

Fig. 7. (a) TRPL decay curves of NaCl-HTS (λ_{em} = 445 nm, and λ_{ex} = 310 nm), and (b) KCl-HTS (λ_{em} = 470 nm, and λ_{ex} = 310 nm).

It is known to the community that the fluorescence properties of materials can also be affected by high pressure [42–45]. In this work, the pressure-dependent PL spectra (up to 25.3 GPa) were carried out on NaCl-HTS (Fig. 8), and the pressure-sensitive fluorescence evolution of the sample is clearly revealed. In Fig. 8a, the PL intensity is decreased with increasing the pressure from atmospheric pressure (1 atm) to the external pressure of 5.9 GPa. Regarding Fig. 8b, the intensity is then greatly increased to its maximum, as the pressure is further raised up to as high as 25.3 GPa, corresponding to the enhancement in the brightness of the fluorescence photographs shown in the circles. The initial decrease in PL intensity may be ascribed to the quenching of the charge transfer transition (CTT) band by pressure; the CTT involves the filled 2p orbital of oxygen whose electron cloud is susceptible to external pressure [44]. The following increase in PL intensity may be attributed to the distortion in oxygen-based structures at high pressure, and similar effects were also observed and addressed in Ref [45]. This pressure-dependent PL spectra not only illustrate the enhancement effect under high pressure, but also confirm the optical property of the HCl-treated NaCl sample.

Based on the blue and blue-green band PL emissions from NaCl-HTS

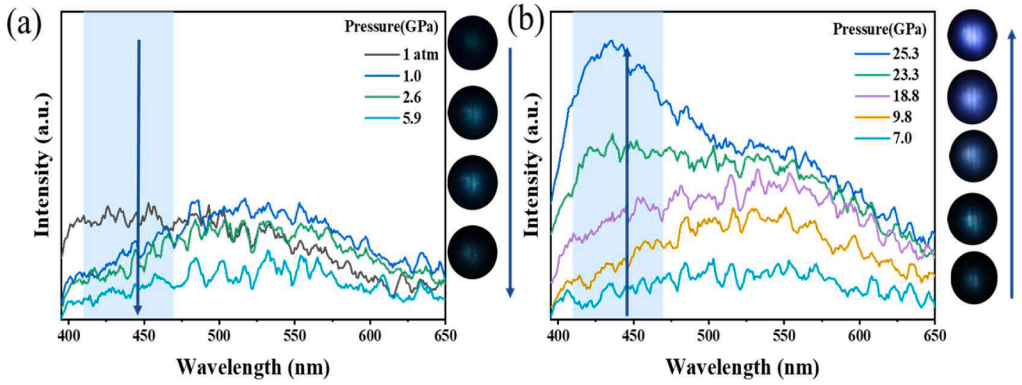

Fig. 8. (a-b) PL spectra of NaCl-HTS under pressure. Arrows indicate the evolution of the PL spectra as a function of pressure. Circles are the corresponding fluorescence photographs.

and KCl-HTS, the single-element LEDs were also synthesized by combining the samples with a commercially customized 300 nm LED chip (Beyond Optoelectronics Co. Ltd., Shenzhen, China). As shown in Fig. 9, the working LEDs emit a bright blue and blue-green light, respectively. The Commission Internationale de l'Eclairage (CIE) color coordinates of the fabricated LEDs are (0.25, 0.26) and (0.26, 0.29), the CCT are 17,573 K and 14,544 K, as well as the CRI of the LEDs are as high as 90.9 and 90.6, respectively.

Note that the emission spectra of Figs. 4 and 9 are different. In details, the PL spectra for NaCl-HTS and KCl-HTS crystals are peaked at 445 nm and 470 nm, respectively (Fig. 4), while the Electroluminescence (EL) spectra of the fabricated LEDs are peaked at 430 nm and 450 nm, respectively (Fig. 9). The origin of the differences between these two experiments is mainly as following: the PL spectrum (Fig. 4) was obtained under the monochromatic light excitation with a wavelength of 295 nm. While, the EL spectrum (Fig. 9) was collected via the commercial 300 nm LED chip that was driven by a current, and its excitation wavelength was a broad range, instead of a single value.

Finally, to demonstrate the adjustability on the hue of the HCl-treated samples, the PL spectra were systematically collected on NaCl-HTS, with a careful manipulation of the excited wavelength (Fig. 10a). The variation in the hue is also clearly illustrated in Fig. 10b where the corresponding CIE coordinates are plotted.

3. Conclusions

NaCl-HTS and KCl-HTS materials have successfully been fabricated, by treating the pristine sodium chloride and potassium chloride crystals in hydrochloric acid, via the hydrothermal synthesis method. Remarkably, photoluminescence emissions have been revealed in these HCl-treated materials, compared to the fact that pristine crystals have no PL emissions. Through NMR spectra, the oxygens have been identified in the HCl-treated phosphor, while none of the oxygens have been shown in the pristine sample. The crystal structural information has further been confirmed by the single crystal XRD experiments. The introduction of the oxygen plays an important role as defects in the perfectly orientated NaCl crystals, inducing a new energy band that is responsible for the blue-band PL emission. The fluorescence enhancement on NaCl-HTS under high pressure is also revealed. Single-element LEDs based on NaCl-HTS and KCl-HTS have also been manufactured, fulfilling blue and blue-green emissions, respectively. We believe the scheme proposed in this work that includes a simple treatment on cost efficient starting materials, together with its underlying physics is of significance in photoluminescence related applications, such as solid state lighting, etc.

3.1. Experimental section

Materials and Chemicals: sodium chloride (NaCl, Kermel, 99.5 %), potassium chloride (KCl, Kermel, 99.5 %), hydrochloric acid (HCl, 37 wt % in water, Sinopharm Chemical Reagent Co., Ltd., China) were the starting reagents. All chemicals were used without further purification, unless otherwise stated.

Synthesis – NaCl: An amount of 176.38 mg (3 mmol) 99.5 % NaCl were added in a polytetrafluoroethylene (PTFE) container with 4.0 mL of 37 % hydrochloric acid. The container was placed in a muffle furnace and kept at 180 °C for 10 h. Crystals were obtained by slowly cooling the solution down to room temperature over the course of 30 h. Crystals of NaCl could be separated by immediate filtration and washed with methanol. The product yields were between 89.85 mg and 139.75 mg.

Synthesis – KCl: An amount of 223.65 mg (3 mmol) 99.5 % KCl were added in a polytetrafluoroethylene (PTFE) container with 4.0 mL of 37 % hydrochloric acid. The container was placed in a muffle furnace and kept at 180 °C for 10 h. Crystals were obtained by slowly cooling the solution down to room temperature over the course of 30 h. Crystals of KCl could be separated by immediate filtration and washed with methanol. The product yields were between 70.45 mg and 118.15 mg.

3.1.1. Characterization

The steady-state photoluminescence (PL) spectra and photoluminescence excitation (PLE) spectra were measured on the picosecond time-resolved fluorescence spectrometer (Pico-1000, Dalian institute of chemical physics, Chinese academy of sciences) with a photomultiplier tube operating at 1000 V, and a 150-W Xe lamp was used as the excitation lamp. The time-resolved PL measurements (TRPL) were excited by frequency-adjustable picosecond laser pulses at 310 nm, collected by the Pico-1000 spectrometer with laser.

The powder X-ray diffraction (PXRD) patterns were measured using an Rigaku Smart Lab 9 kWX-ray 150 Powder diffractometer (Tokyo), with a scanning speed of 5°/min.

The X-ray photoelectron spectrometer (XPS) used was a ESCALAB 250Xi (Thermo Fisher).

The scanning electron microscope (SEM) was performed using a SU3500 (Hitachi).

The single crystal X-ray diffraction (SC-XRD) were measured using an Rigaku XtaLAB-Synergy-R (Japan).

The solid-state magic angle spinning nuclear magnetic resonance (SS-MAS-NMR) spectra of ^{17}O, and ^{1}H were obtained on Bruker-Biospin 500 MHz AVANCE NEO system with a magnetic field strength of 14.09 T For ^{1}H, the spin rate of the samples was 20 kHz, the $\pi/2$ pulse was 3.5 μs, with the recycle delay of 5 s, and the chemical shift was calibration at 1.74 ppm with adamantane. For ^{17}O, the spin rate of the samples was 20k Hz, the $\pi/12$ pulse was 0.27 us, with the recycle delay of 1 s, and the chemical shift was calibration at 0 ppm with $H_2^{17}O$.

The in-situ high pressure PL was excited with a 355 nm semiconductor laser with an output power of 10 mV, and the spectra were collected by an optical fiber spectrometer (Ocean Optics, QW65000);

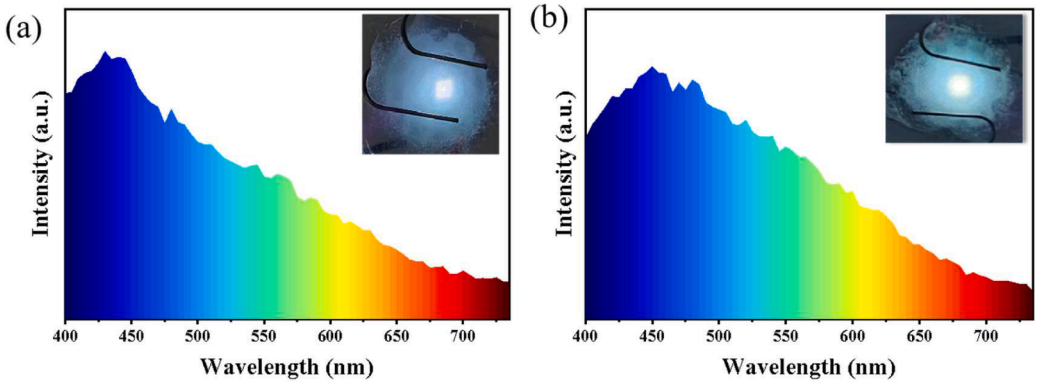

Fig. 9. Electroluminescence spectrum of the fabricated LED based on (a) NaCl-HTS, and (b) KCl-HTS, under an injection current of 80 mA. Inset: physical LED pictures.

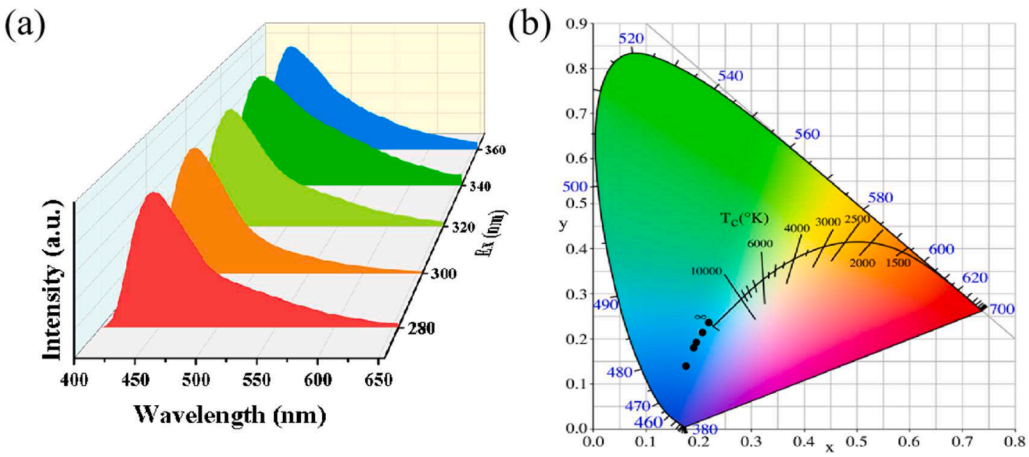

Fig. 10. (a) Normalized PL spectra of NaCl-HTS, with a variety of excitation wavelengths ranging from 280 to 360 nm. (b) CIE color coordinates corresponding to the PL spectra in (a).

the fluorescence photographs were taken by a camera (Canon Eos 5D mark II) installed on a microscope (Ecilipse TI-U, Nikon); the high pressure was generated by a symmetric diamond anvil cell (DAC) with a culet size of 400 um.

The LED devices were prepared by combining UV–LED chips (300 nm) with the prepared NaCl-HTS and KCl-HTS samples. The prepared phosphors were first mixed with epoxy resin thoroughly. The bubbles in the silicone were then removed through a vacuum chamber and the mixture was applied to the LED chip, and finally cured at 80 °C for 2 h to manufacture the LED devices.

CRediT authorship contribution statement

Xue Yang: Writing – original draft, Investigation, Formal analysis. **Tao Xiong:** Investigation, Funding acquisition. **Yida Zhou:** Investigation. **Shutao Xu:** Resources. **Zongqing Jin:** Investigation. **Guanjun Xiao:** Resources. **Bo Zou:** Resources. **Qingqin Ge:** Formal analysis, Investigation, Resources. **Nannan Shi:** Investigation. **Cheng Sun:** Writing – review & editing, Writing – original draft, Resources, Project administration, Funding acquisition, Conceptualization. **Ting Wang:** Formal analysis. **Yinan Zhang:** Formal analysis.

Declaration of competing interest

The authors declare that they have no known competing financial interests or personal relationships that could have appeared to influence the work reported in this paper.

Acknowledgements

C. Sun acknowledges support by Grant Number DLUXK-2024-YB-010 from the Interdisciplinary Project of Dalian University. T. Wang acknowledges support by Grant Number JYTQN2023102 from the Youth Research Programme of the Education Department of Liaoning Province, China. T. Xiong acknowledges support by Grant Number JYTMS20230381 from the Basic Research Programme of the Education Department of Liaoning Province, China. The authors gratefully acknowledge Ms. Yanhui Wang for analysis of the XPS results.

Supplementary materials

Supplementary material associated with this article can be found, in the online version, at doi:10.1016/j.apmt.2025.102736.

Data availability

Essential data are provided in the main text. Additional data can be available from the corresponding author upon reasonable request.

References

[1] H. Kim, S.Z. Uddin, D.H. Lien, M. Yeh, N.S. Azar, S. Balendhran, T. Kim, N. Gupta, Y. Rho, C.P. Grigoropoulos, K.B. Crozier, A. Javey, Actively variable-spectrum optoelectronics with black phosphorus, Nature 596 (2021) 232–253.
[2] J.J. Luo, X.M. Wang, S.R. Li, J. Liu, Y.M. Guo, G.D. Niu, L. Yao, Y.H. Fu, L. Gao, Q. S. Dong, C.Y. Zhao, M.Y. Leng, F.S. Ma, W.X. Liang, L.D. Wang, S.Y. Jin, J.B. Han, L.J. Zhang, J. Etheridge, J.B. Wang, Y.F. Yan, E.H. Sargent, J. Tang, Efficient and stable emission of warm-white light from lead-free halide double perovskites, Nature 563 (2018) 541–545.
[3] Y.H. Kim, Y.X. Zhai, H.P. Lu, X. Pan, C.X. Xiao, E.A. Gaulding, S.P. Harvey, J. J. Berry, Z.V. Vardeny, J.M. Luther, M.C. Beard, Chiral-induced spin selectivity enables a room-temperature spin light-emitting diode, Science 371 (2021) 1129–1133.
[4] P. Sutter, S. Wimer, E. Sutter, Chiral twisted van der Waals nanowires, Nature 570 (2019) 354–357.
[5] Y. Zhan, B. Shang, M. Chen, L.M. Wu, One-step synthesis of silica-coated carbon dots with controllable solid-state fluorescence for white light-emitting diodes, Small 15 (2019) 19011161.
[6] R. Chen, K. Cao, Y.W. Wen, F. Yang, J. Wang, X. Liu, B. Shan, Atomic layer deposition in advanced display technologies: from photoluminescence to encapsulation, Int. J. Extreme Manuf. 6 (2024) 022003.
[7] R. Shang, F. Yang, G. Gao, Y. Luo, H. You, L. Dong, Bioimaging and prospects of night pearls-based persistence phosphors in cancer diagnostics, Exploration 4 (2024) 20230124.
[8] D.A. Gálico, C.M.S. Calado, M. Murugesu, Lanthanide molecular cluster-aggregates as the next generation of optical materials, Chem. Sci. 14 (2023) 5827–5841.
[9] C.H. Kang, Y. Wang, O. Alkhazragi, H. Lu, T.K. Ng, B.S. Ooi, Down-converting luminescent optoelectronics and their applications, APL Photonics 8 (2023) 020903.
[10] G. Kranzelbinder, G. Leising, Organic solid-state lasers, Rep. Prog. Phys. 63 (2000) 729–762.
[11] Y. Fujimoto, M. Nakatsuka, Optical amplification in bismuth-doped silica glass, Appl. Phys. Lett. 82 (2003) 3325–3326.
[12] J.X. Zhao, Y. Zhang, T.A. Wang, L. Guan, G.Y. Dong, Z.Y. Liu, N. Fu, F.H. Wang, X. Li, Preparation and luminescent modulation of $KGaSiO_4$:Eu^{3+}phosphors using for multiple anti-counterfeiting, Ceram. Int. 49 (2023) 29505–29511.
[13] S.P. Ying, B.M. Chen, W.L. Tseng, Thin-film luminescent solar concentrators using inorganic phosphors, IEEE Trans. Electron Devices 66 (2019) 2290–2294.
[14] Q.R. Jin, R. Wu, Y.X. Pan, Y.H. Ding, H.Z. Lian, J. Lin, L.Y. Li, Dual-emissive luminescence in OIHMH single crystals: tunable red-green emissions via Mn^{2+} doping and theoretical insights, Chem. Sci. 15 (2024) 17173–17182.
[15] W.H. Jin, Q. Wang, M. Chen, Q. Zhang, D.H. Qu, Color-tunable luminescent materials via a CB[8]-based supramolecular assembly strategy, Mater. Chem. Front. 5 (2021) 2347–2352.
[16] P. Felbier, J.H. Yang, J. Theis, R.W. Liptak, A. Wagner, A. Lorke, G. Bacher, U. Kortshagen, Highly luminescent ZnO quantum dots made in a nonthermal plasma, Adv. Funct. Mater. 24 (2014) 1988–1993.
[17] H. Zhang, H.Q. Zhang, A.Z. Pan, B. Yang, L. He, Y.S. Wu, Rare earth-free luminescent materials for WLEDs: recent progress and perspectives, Adv. Mater. Technol. 6 (2021) 2000648.
[18] K. Dave, W.T. Huang, R.S. Liu, All inorganic lead-free zero-dimensional metal halide luminescent materials and applications, Crystals 13 (2023) 499.

[19] M. Sessolo, L. Gil-Escrig, G. Longo, H.J. Bolink, Perovskite luminescent materials, Top. Curr. Chem. 374 (2016) 52.

[20] X.Y. Chen, X.Y. Huang, Full-visible-spectrum white LEDs enabled by a blue-light-excitable cyan phosphor, ACS Appl. Mater. Interfaces 16 (2024) 57365–57376.

[21] X.Y. Chen, X.Y. Huang, Highly efficient and thermally stable broadband green-emitting $BaY_2Sc_2Al_2SiO_{12}:Ce^{3+}$ phosphors enabling warm-white LEDs with high luminous efficacy and high color rendering index, J. Mater. Chem. C 12 (2024) 16741.

[22] C. Xian, X.Y. Chen, X.Y. Huang, High-performance green-emitting $Ca_2YScAl_2Si_2O_{12}:Ce^{3+}$ garnet phosphors and their applications in high-quality blue-chip-pumped white LEDs, J. Mater. Chem. C 12 (2024) 12378.

[23] X.Y. Chen, X.Y. Huang, Ce^{3+}-activated $SrLu_2Al_3ScSiO_{12}$ cyan-green-emitting garnet-structured inorganic phosphor materials toward application in blue-chip-based phosphor-vonverted dolid-dtate ehite lighting, Inorg. Chem. 63 (2024) 5743–5752.

[24] J.M. Chan, B. Devakumar, H.Z. Gao, X.Y. Huang, Efficient violet-light-excitable blue-cyan-emitting $Ca_2YHf_2GaAl_2O_{12}:ce^{3+}$ garnet phosphors enable high-color-rendering full-spectrum warm-white LEDs, Mater. Today Chem. 40 (2024) 102218.

[25] Y. Cheng, D.H. Ren, H. Zhang, X.L. Cheng, First-principle study of the structural, electronic and optical properties of defected amorphous silica, J. Non-Cryst. Solids 416 (2015) 36–43.

[26] B. Berzina, L. Trinkler, J. Sils, K. Atobe, Luminescence mechanisms of oxygen-related defects in AlN, Radiat. Eff. Defects Solids 157 (2002) 1089–1092.

[27] Q.Y. Bai, P.L. Li, Z.J. Wang, S.C. Xu, T. Li, Z.P. Yang, Z. Xu, Inducing tunable host luminescence in Zn_2GeO_4 tetrahedral materials via doping Cr^{3+}, Spectrochim Acta A 199 (2018) 179–188.

[28] X.J. Kang, W. Lü, Z.N. Zhu, Q.W. Pan, Multiple defects induced near-infrared self-luminescence of (Ca,Sr) $LaMgTaO_6$ double perovskite phosphor, Ceram. Int. 49 (2023) 32719–32726.

[29] Y.L. Huang, W.B. Fan, Y.H. Hou, K.X. Guo, Y.F. Ouyang, Z.W. Liu, Effects of intrinsic defects on the electronic structure and magnetic properties of $CoFe_2O_4$: a first-principles study, J. Magn. Magn. Mater. 429 (2017) 263–269.

[30] K.K. Thejas, S.C. Lal, R.T. Parayil, S.K. Gupta, S. Das, Defect-induced new persistent cyan-emitting rare-earth-free phosphors for dynamic anti-counterfeiting and plant-growth LED applications, J. Mater. Chem. C 13 (2025) 3554.

[31] A. Balhara, S.K. Gupta, B. Modak, M. Abraham, A.K. Yadav, H.V. Annadata, S. Das, N.S. Rawat, K. Sudarshan, Synergy between structural rigidity and cluster defects in a bright near-infrared Cr^{3+}-based phosphor for excellent thermal stability and long afterglow, J. Mater. Chem. C 12 (2024) 9716.

[32] A. Balhara, S.K. Gupta, K. Sudarshan, S. Patra, A. Chakraborty, S. Chakraborty, $ZnAl_2O_4:Er^{3+}$ upconversion nanophosphor for SPECT imaging and luminescence modulation via defect engineering, ACS Appl. Bio Mater. 7 (2024) 2354–2366.

[33] R.T. Parayil, S.K. Gupta, M. Mohapatra, A review on defect engineered NIR persistent luminescence through transition metal ion (Cr, Mn, Fe and Ni) doping: wider perspective covering synthesis, characterization, fundamentals and applications, Coord. Chem. Rev. 522 (2025) 216200.

[34] M. Hochheim, T. Bredow, Band-edge levels of the NaCl(100) surface: self-consistent hybrid density functional theory compared to many-body perturbation theory, Phys. Rev. B 97 (2018) 235447.

[35] R.T. Poole, J.G. Jenkin, J. Liesegang, R.C.G. Leckey, Electronic band structure of the alkali halides. I. Experimental parameters, Phys. Rev. B 11 (1975) 365–385.

[36] W. He, H.W. Li, H.Q. Zhou, H.K. Zhao, H. Wang, X.H. Shi, Effect of defects on the electronic structure of a PbI_2/MoS_2 van der Waals heterostructure: a first-principles study, Sci. China Phys. Mech. 63 (2020) 234611.

[37] D. Wickramaratne, C.E. Dreyer, J.X. Shen, J.L. Lyons, A. Alkauskas, C.G. Van de Walle, Deep-level defects and impurities in InGaN alloys, Phys. Status Solidi B 257 (2020) 1900534.

[38] S. Wang, L.J. Wu, Z.Q. Wang, Z.Y. Qian, L.H. He, Y. Liu, L.H. Shen, Effect of vacancy defect on the structural and electrical properties of single-walled silicon nanotube, Mater. Today Commun. (2024) 40, https://doi.org/10.1016/j.mtcomm.2024.109536.

[39] T.J. Whitcher, N.A. Talik, K. Woon, N. Chanlek, H. Nakajima, T. Saisopa, P. Songsiriritthigul, Determination of energy levels at the interface between O_2 plasma treated ITO/P3HT:PCBM and PEDOT:PSS/P3HT:PCBM using angular-resolved x-ray and ultraviolet photoelectron spectroscopy, J. Phys. D: Appl. Phys. 47 (2014) 055109.

[40] Q. Hu, H.D. Tang, H.Z. Wu, S.H. Pan, Y.Q. Xu, W.H. Jiang, L.J. Wang, W. Jiang, Facile preparation of highly efficient Te^{4+}-doped Rb_2SnCl_6 perovskites for white light-emitting diodes, J. Lumin. 261 (2023) 119904.

[41] N. Pathak, S.K. Gupta, P.S. Ghosh, A. Arya, V. Natarajan, R.M. Kadam, Probing local site environments and distribution of manganese in SrZrO3:Mn; PL and EPR spectroscopy complimented By DFT calculations, RSC Adv. 5 (2015) 17501.

[42] C. Hernandez, S.K. Gupta, J.P. Zuniga, J. Vidal, R. Galvan, M. Martinez, H. Guzman, L. Chavez, Y.B. Mao, K. Lozano, Performance evaluation of Ce^{3+} doped flexible PVDF fibers for efficient optical pressure sensors, Sensor Actuat. A-Phys. 298 (2019) 111595.

[43] C. Hernandez, S.K. Gupta, J.P. Zuniga, J. Vidal, R. Galvan, H. Guzman, L. Chavez, K. Lozano, Y.B. Mao, High pressure responsive luminescence of flexible Eu^{3+} doped PVDF fibrous mats, J. Mater. Sci. Technol. 66 (2021) 103–111.

[44] S.K. Gupta, J.P. Zuniga, M. Pokhrel, Y.B. Mao, High pressure induced local ordering and tunable luminescence of $La_2Hf_2O_7:Eu^{3+}$ nanoparticles, New J. Chem. 44 (2020) 5463.

[45] S.K. Gupta, H. Abdou, Y.B. Mao, Appearance of new photoluminescence peak and spectral evolution of Eu^{3+} in $La_2Zr_2O_7$ nanoparticles at high pressure, J. Alloys Compd. 870 (2021) 159438.